Surface reconstruction induced highly efficient N-doped carbon nanosheet supported copper cluster catalysts for dimethyl carbonate synthesis

Yongli Pei [a,b], Yanhong Quan [a,b], Xuhui Wang [a,b], Jinxian Zhao [a,b], Ruina Shi [a,b], Zhong Li [a,b], Jun Ren [a,b,*]

[a] *State Key Laboratory of Clean and Efficient Coal Utilization, Taiyuan University of Technology, Taiyuan 030024, China*
[b] *Key Laboratory of Coal Science and Technology (Taiyuan University of Technology), Ministry of Education, China*

ARTICLE INFO

ABSTRACT

N-doped hierarchical porous carbon nanosheets-supported copper catalysts (Cu/NCNS-*x*) were fabricated to solve the problem of deactivation caused by the leaching, agglomeration and oxidation of Cu nanoparticles (NPs) in the dimethyl carbonate (DMC) synthesis. The optimal Cu/NCNS-12 exhibited superb activity and stability without obvious deactivation after 10 cycles. The nanosheet structure produced new defects resulting in Cu reconstruction during the reaction process, while the strong interaction between Cu^0 and N atoms greatly inhibited the oxidation of Cu^0. The reconstruction of Cu was stimulated at above 100 °C, regardless of atmosphere, solvent types, pressure and rotation speed. The mechanism was elaborated that the initial Cu NPs (11 nm) migrated and then was trapped into newly created defects, finally formed into clusters (0.91 nm) as well as single-atom sites. This work provides profound potential in understanding metal reconstruction and developing a promising synthetic strategy of metal cluster catalysts.

1. Introduction

In the field of heterogeneous catalysis, the liquid-phase intermittent reaction in an autoclave has been shown to have numerous advantages because of its higher heat transfer efficiency, high yield and simple equipment; and thus, it is widely used in the hydrogenation of aromatics [1], hydrodeoxygenation of aromatic carbonyls [2], N-alkylation of amines [3] and so on. However, the leaching or aggregation of active metal nanoparticles (NPs) frequently occurs during the recycles, which causes irreversible deactivation of metal-supported catalysts. Recently, a variety of strategies have been explored to improve the stability of metal NPs, such as the fabrication of small-sized metal NPs via sol immobilization [4], the creation of an enhanced metal-support interaction by heteroatom doping on the support [5,6] as well as the synthesis of a single-metal sites material with high loading [3].

Dimethyl carbonate (DMC) is an important and environmentally friendly chemical intermediate to meet the growing demand for a clean and sustainable energy supply [7]. Among several routes for DMC synthesis, the liquid-phase oxidative carbonylation of methanol has attracted much attention with the advantages of a high utilization rate of carbon source, moderate operating conditions and environmental

benefits [8]. However, the carbon-supported Cu catalysts unsurprisingly suffer from the leaching and aggregation of Cu NPs in the harsh reaction conditions with high temperature, high pressure as well as severe stirring [9–11]. In addition, it also perhaps undergoes the oxidation of Cu^0 species, which was considered as another major deactivation factor [12]. In our previous studies, several strategies have been attempted to solve the deactivation problem caused by these reasons. For instance, encapsulating Cu NPs with hollow porous carbon spheres or mesoporous carbon materials [13,14]. Besides, the introduction of N species in the carbon framework or sulfonic acid groups and oxygen-containing groups on the surface of carbon materials leads to an anchoring effect on Cu NPs [9,12,15]. Great progress has been made via these methods, yet still unsatisfactory. Therefore, developing a novel synthetic method capable of stabilizing metal species without sacrificing their activity remains highly desirable, yet challenging.

The great success of graphene has stimulated the rise of two-dimensional (2D) materials [16]. The 2D nanosheets present unusual layered structure, abundant and accessible active sites, as well as unique electronic and optical properties [17]. In particular, hierarchical porous carbon nanosheets (CNS), combining both 2D morphology and micro-, meso- and macroporous architectures, have recently attracted

---

tremendous attention in various areas. Their open pores and layered structure result in the excellent confining effect of metal NPs, high exposure of active sites as well as efficient transport of electrons and mass [18–20]. These combined properties enable CNS to be a proper support material to prevent the metal NPs from leaching and aggregating. As reported, the Rh, Au, Pt and Co loaded on the CNS exhibited outstanding catalytic performance in the reduction of 4-NP, ORR, electro-oxidation of methanol and hydrolysis of NaBH$_4$, respectively [21–24]. Furthermore, the incorporation of nitrogen species in the CNS (NCNS) was employed as the most promising method to improve the stabilization of metal NPs such as Pd, Ru, Fe$_3$C and bimetallic NiCo [25–28]. More importantly, it can also tune the electronic structure of metal species, further facilitating the formation and stabilization of metallic species [6,29], which therefore resulted in enhanced catalytic activity and durability.

In the present work, it was proposed that the CNS and NCNS act as alternative support materials for stabilizing Cu NPs to inhibit the leaching, aggregation and oxidation of active copper species to improve catalytic activity and stability in the DMC synthesis. Comprehensive characterization techniques revealed the anti-leaching and anti-aggregation mechanism for Cu NPs derived from the hierarchical porous structure of CNS. It also illustrated the promotion effect of nitrogen species on the formation and stabilization of active Cu^0 species with high anti-oxidation properties. In conclusion, a Cu/NCNS catalyst with excellent activity and stability was obtained by tuning the N-doping concentration.

2. Experimental procedures

2.1. Chemicals

Magnesium citrate (Mg$_3$(C$_6$H$_5$O$_7$)$_2$·9H$_2$O), potassium citrate (K$_3$C$_6$H$_5$O$_7$·H$_2$O), ammonium oxalate ((NH$_4$)$_2$C$_2$O$_4$·H$_2$O), copper(II) nitrate (Cu(NO$_3$)$_2$·3H$_2$O) and methanol (CH$_3$OH) were purchased from Aladdin Chemistry Co., Ltd. and used without further purification. CO (>99.99%) and O$_2$ (>99.99%) were purchased from the Jining Xieli Special Gases Co., Ltd.

2.2. Preparation procedures

The NCNS samples were prepared according to a reported procedure with a minor modification [30]. A mixture of K$_3$C$_6$H$_5$O$_7$·H$_2$O, Mg$_3$(C$_6$H$_5$O$_7$)$_2$·9H$_2$O and (NH$_4$)$_2$C$_2$O$_4$·H$_2$O (mass ratio 1:4:x) was ground and calcined at 850 °C for 2 h in a N$_2$ flow (100 mL·min^{-1}). After cooling to room temperature, the resulting black solid was thoroughly washed with large amounts of 2 M HCl solution, followed by washing with deionized water to pH around 7, and dried at 70 °C for 12 h. The obtained material was named NCNS-x (x = 4, 8 and 12). The CNS sample was prepared via the same method without the addition of (NH$_4$)$_2$C$_2$O$_4$·H$_2$O.

The Cu/CNS and Cu/NCNS-x catalysts were prepared using a wet-impregnation method and the process was described as follows: 0.093 g Cu(NO$_3$)$_2$·3H$_2$O was dissolved in 15 mL deionized water. Subsequently, 0.22 g support material (CNS or NCNS-x) was dispersed ultrasonically into the homogeneous solution. After that, the mixed solution was stirred at 80 °C until the solvent had evaporated, followed by drying at 80 °C for 8 h before reduction at 400 °C in H$_2$ diluted with N$_2$ for 2 h. The finally obtained catalyst samples were denoted Cu/CNS or Cu/NCNS-x (x = 4, 8 and 12).

2.3. Catalytic tests

The catalytic reaction was performed using a 25 mL stainless-steel stirred autoclave. Typically, a mixture of catalyst and methanol was placed in the reactor. The reactor was sealed and purged three times with CO, and then pressurized to 3.0 MPa with CO and O$_2$ (P_{CO}:P_{O_2} =

2:1). The reactor was heated to 120 °C and maintained for 1.5 h. When the reaction was completed, the product was analyzed using a Haixin GC-950 instrument equipped with a flame ionization detector. The recycling stability tests of catalysts were carried out under the same conditions as those used in the activity tests. The by-products included dimethoxy methane (DMM) and methyl formate (MF). The catalytic performance of the catalyst can be expressed in terms of the methanol conversion (C$_{MeOH}$, %), the DMC selectivity (S$_{DMC}$, %), space-time yield of DMC (STY$_{DMC}$, mg/(g·h)), the DMM selectivity (S$_{DMM}$, %), and the MF selectivity (S$_{MF}$, %), and these were calculated as follows:

$$C_{MeOH} = \frac{n_{reacted\ MeOH}}{n_{total\ MeOH}} \times 100\%,$$

$$S_{DMC} = \frac{2 \times n_{produced\ DMC}}{n_{reacted\ MeOH}} \times 100\%,$$

$$S_{DMM} = \frac{3 \times n_{produced\ DMM}}{n_{reacted\ MeOH}} \times 100\%,$$

$$S_{MF} = \frac{2 \times n_{produced\ MF}}{n_{reacted\ MeOH}} \times 100\%,$$

$$STY_{DMC} = \frac{m_{produced\ DMC}}{m_{cat} \times t}.$$

2.4. Characterization techniques

The Brunauer-Emmet-Teller (BET) surface area and interstitial porous structure were measured using a Beishide 3H-2000PS2 analyzer. The morphology, structures and composition of the as-obtained sample were examined with a field emission scanning electron microscope (FE-SEM, Hitachi SU8010), transmission electron microscope (TEM, JEOL JEM2100F), aberration-corrected high angle annular dark-field scanning transmission electron microscope and elemental mapping (HAADF-STEM, JEM ARM 300F). Elemental analysis (EA) was performed on a CHN elemental analyzer (Elementar EL III).

The actual loading of Cu in the catalysts was analyzed using atomic absorption spectrometry (AAS, Varian SpectrAA-220). X-ray diffraction (XRD) results were obtained on a Rigaku D/max 2500 diffractometer and used to determine the species of Cu. X-ray photoelectron spectra (XPS) were obtained using a Thermo ESCALAB 250Xi analyzer. All binding energy (BE) values were calibrated using the C 1s peak at 284.6 eV. Raman spectra were obtained on a Renishaw 21000. X-ray adsorption fine structure (XAFS) measurement, including X-ray absorption near-edge structure (XANES) and extended X-ray absorption fine structure (EXAFS) for the catalysts were performed on the Soft X-ray Micro-characterization Beamline (SXRMB) at the Canadian Light Source.

The temperature-programmed reduction (H$_2$-TPR), H$_2$-N$_2$O titration and CH$_3$OH temperature-programmed desorption (CH$_3$OH-TPD) were measured using a Tianjin Xianquan TP-5080 instrument. For H$_2$-TPR, 30 mg samples were treated with Ar at 300 °C for 30 min to remove physisorbed moisture. Then, the samples were reduced in 5 vol% H$_2$/Ar at a heating rate of 10 °C/min up to 500 °C. For the H$_2$-N$_2$O titration, the pretreated samples were reduced in 5 vol% H$_2$/Ar from ambient temperature to 500 °C. After cooling to 50 °C in Ar, pure N$_2$O was introduced to oxidize surface metallic Cu to Cu$_2$O. Then, the samples were purged with Ar to remove the residual N$_2$O. Subsequently, under a flow of 5 vol% H$_2$/Ar, the resulting sample was reheated to 500 °C to reduce surface Cu$_2$O to metallic Cu. From that, the dispersion (D_{Cu}) of Cu can be obtained [31]. For CH$_3$OH-TPD, the samples were first degassed at 300 °C under He flow for 0.5 h, and then the CH$_3$OH carried by He was introduced for 1 h using a bubble method and then swept with He to remove physically adsorbed molecules. The temperature of samples was raised to 300 °C under He to obtain the desorbed profile.

2.5. Density functional theory (DFT) calculations

DFT calculations were employed to provide theoretical support, and the detailed computational methods and models are given in the Supporting Information.

3. Results

3.1. Oxidative carbonylation of methanol

The catalytic results for oxidative carbonylation of methanol on Cu/CNS and Cu/NCNS catalysts are shown in Fig. 1 and Table S1. The CNS and NCNS-12 were not active. In all cases, the Cu/NCNS catalysts exhibited a much better catalytic activity than that of Cu/CNS, and the initial activity first increased then decreased with increasing N-doping content in the Cu/NCNS catalysts. The highest initial activity (STY_{DMC}, 3227 mg/(g·h)) was obtained on Cu/NCNS-8, which was nearly two times higher than that of the Cu/CNS catalyst. Moreover, it also was much higher than that of Cu/MSC [14], Cu/NCNT200 [11] and Cu/HPC-900 [32] catalysts. Distinctly, the design strategy of Cu/NCNS catalysts has profound potential in preparing an effective candidate for DMC synthesis.

Stability tests were carried out under the same reaction conditions using the recycled spent catalysts after washing with methanol followed by drying in vacuum for 36 h. The test results for different catalysts are also presented in Fig. 1 and Table S1. In all cases, the stability was found to increase steadily with the increasing N-doping content. For the Cu/CNS, Cu/NCNS-4 and Cu/NCNS-8 catalysts, the loss rate of STY_{DMC} was 77.9%, 69.9% and 36.8% after 10 reaction cycles, respectively. Surprisingly, although Cu/NCNS-8 presented a superior initial activity

Fig. 1. (a) Methanol conversion and DMC selectivity and (b) space time yield of DMC over Cu/CNS and Cu/NCNS catalysts as a function of cycle times.

(3227 mg/(g·h)), the Cu/NCNS-12 catalyst maintained its comparatively high activity with the STY_{DMC} of 2197 mg/(g·h) after 10 cycle tests, even slightly higher than the initial activity (2148 mg/(g·h)). To our knowledge, this is almost the best activity and durability among all the carbon-supported copper catalysts reported in the literature so far [11,14–15,32].

3.2. Characterization of the fresh and spent catalysts

3.2.1. Morphology and textural properties

3.2.1.1. SEM, N_2 physisorption and EA. Fig. 2(a–d) shows that all the fresh catalysts presented an interconnected network of CNS. Nitrogen adsorption tests were undertaken to characterize the textural properties of the sheet-like catalysts. As shown in Fig. S1, Cu/CNS and Cu/NCNS showed similar I/IV-type isotherm and pore size distribution curves, indicative of similar micro/mesoporous structure. As listed in Table 1, all the catalysts had relatively high BET surface areas and pore volumes. However, the Cu/NCNS presented a higher V_{meso}/V_{total} of ~70.0% than that of Cu/CNS (52.7%), indicating that more developed mesopores were produced in the Cu/NCNS catalysts. The difference in the textural structure is resulted from the adding $(NH_4)_2C_2O_4$, acting as a foaming agent to enlarge the pore size during the formation of NCNS [1]. The N content in the bulk of NCNS was measured using EA and shown in Table 2, further confirming the N species was successfully doped.

3.2.1.2. SEM and AAS. As shown in Fig. 2(e–h), the morphology and textural structure of spent Cu/CNS and Cu/NCNS catalysts was not obviously changed after 10 catalytic runs, indicating that the mechanical properties of the resultant catalysts were fairly stable in the harsh reaction conditions. As listed in Table 3, the actual Cu loading detected by AAS in these four catalysts were similar before and after reaction. More importantly, compared with the fresh ones, more than 80% of the initial Cu loading was still retained in the spent catalysts (~8.5 wt%). This finding suggested that the leaching of active copper species was efficiently suppressed for the Cu/CNS and Cu/NCNS catalysts, which will be explained later (Section 4.2).

3.2.2. Size distribution of copper

The catalytic activity of supported Cu catalysts is strongly dependent on the dispersion of active species [33,34], which was investigated using TEM, XRD, H_2–N_2O titration, HAADF-STEM and elemental mapping, and XAFS.

3.2.2.1. TEM, XRD and H_2–N_2O titration. From Fig. 3(a–d), it can be clearly observed that Cu NPs were uniformly dispersed on individual nanosheets. A regular lattice with a phase with interplanar spacings of 0.21 and 0.18 nm can be ascribed to the Cu^0 (111) and (200) phases (JCPDS 04-0836), which corresponded to the strong diffraction peaks at 43.3° and 50.4° in the XRD patterns, respectively (Fig. 4a). Besides, it was noted that a weak peak of Cu_2O (36.4°, JCPDS 05-0667) was also observed in Fig. 4a. It can be therefore concluded that Cu^0 was the main metal species in the Cu/CNS and Cu/NCNS catalysts. In addition, the Cu/NCNS catalysts exhibited a smaller grain size of Cu NPs than Cu/CNS, and Cu/NCNS-8 showed the smallest grain size (10.9 nm) and the highest Cu dispersion of 39.3% as shown in Table 1.

3.2.2.2. TEM, XRD and HAADF-STEM. Surprisingly, completely different from the fresh ones, no noticeable Cu NPs were observed in TEM images of all the spent catalysts (Fig. 3(e–h)). Moreover, the XRD of the spent catalysts (Fig. 4b) indicated that the peaks of Cu^0 and Cu_2O had completely disappeared, while several weak and broad diffraction lines belonging to CuO (JCPDS 44-0706) appeared, which was caused by the oxidation of Cu_2O or Cu^0 during the reaction process. Moreover, as for the Cu/NCNS catalysts, it seemed that there was a clear decrease of
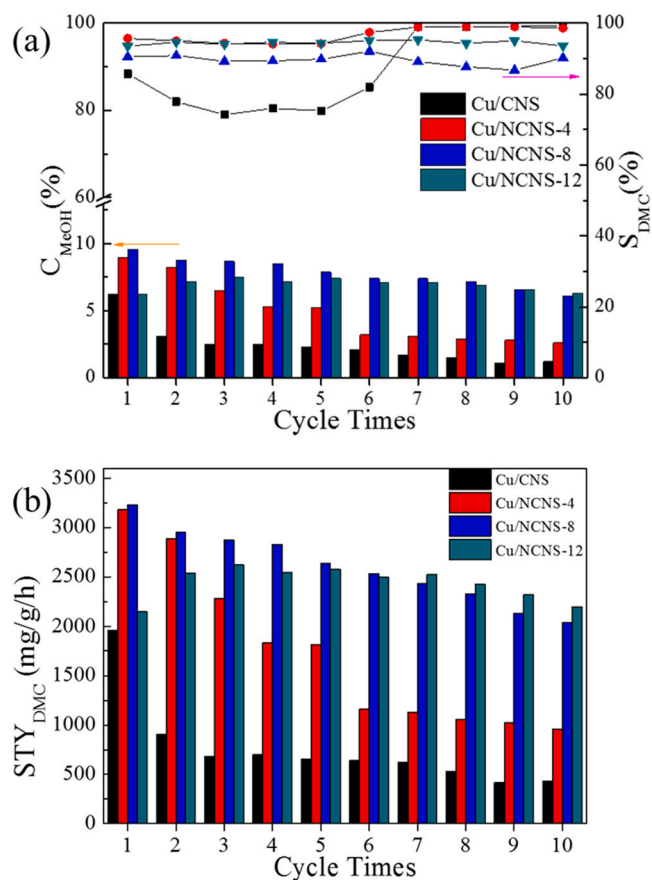
(a) Cu/CNS

(e) Cu/CNS-spent

(b) Cu/NCNS-4

(f) Cu/NCNS-4-spent

(c) Cu/NCNS-8

(g) Cu/NCNS-8-spent
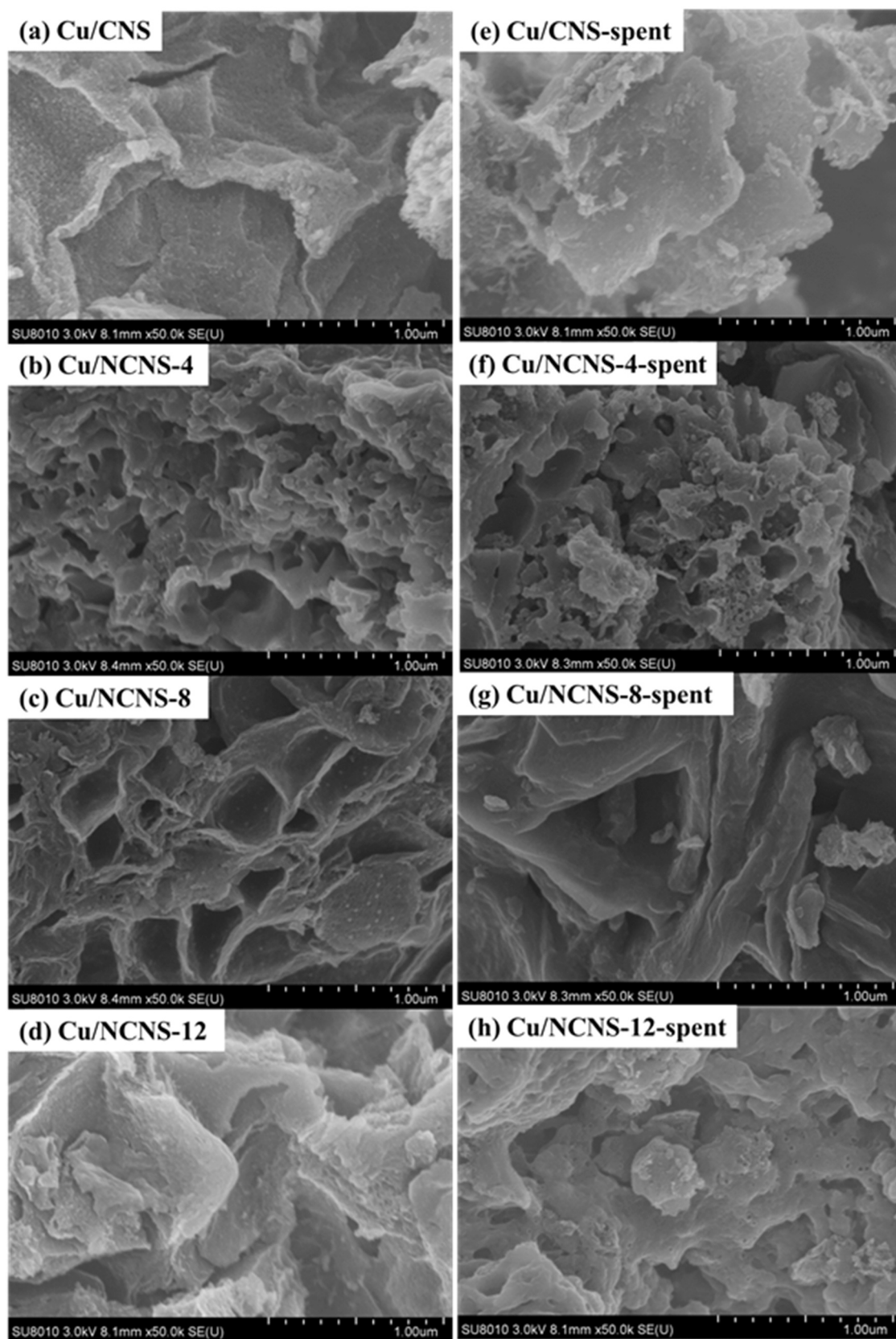
(d) Cu/NCNS-12

(h) Cu/NCNS-12-spent

Fig. 2. SEM images of (a–d) the fresh and (e–h) spent Cu/CNS and Cu/NCNS catalysts.

Table 1
Physical properties and Cu dispersion of Cu/CNS and Cu/NCNS catalysts.

Samples	D_{Cu}[a] (%)	S_{BET}[b] ($m^2 \cdot g^{-1}$)	V_{total}[c] ($cm^3 \cdot g^{-1}$)	V_{micro}[d] ($cm^3 \cdot g^{-1}$)	V_{meso}[e] ($cm^3 \cdot g^{-1}$)	V_{meso}/V_{total} (%)	D[f] (nm)
Cu/CNS	25.8	1468	1.48	0.70	0.78	52.7	3.6
Cu/NCNS-4	33.6	1344	1.49	0.49	1.00	67.1	3.8
Cu/NCNS-8	39.3	1079	1.08	0.26	0.82	75.9	3.8
Cu/NCNS-12	36.9	968	1.01	0.25	0.76	75.2	3.8

[a] Determined by H_2-N_2O.
[b] Specific surface area was calculated using Brumauer-Emmett-Teller (BET) modeling.
[c] Total pore volume was measured by single point adsorption at $P/P_0 = 0.99$.
[d] Micropore volume was measured by the t-plot method.
[e] Mesopore volume was measured by the BJH method.
[f] Most probable apertures calculated by DFT method for Cu/CNS and Cu/NCNS.

Table 2
Carbon, hydrogen, and nitrogen element analysis of the obtained CNS and NCNS materials.

Samples	C (wt%)	O (wt%)	H (wt%)	N (wt%)
CNS	79.8	18.9	1.3	0
NCNS-4	79.3	17.1	1.5	2.1
NCNS-8	75.6	18.5	2.1	3.8
NCNS-12	75.7	18.4	2.0	3.9

the peak intensity of CuO and even absence of CuO for the Cu/NCNS-12 catalyst, indicating that an extremely high dispersion of copper was probably reached after 10 cycles, and a less amount of CuO was observed on the Cu/NCNS-8-spent and Cu/NCNS-12-spent catalysts. Furthermore, the HAADF-STEM image (Fig. 5a) of the spent Cu/NCNS-12 showed many clusters (red circled) and loose individual single atoms (yellow circled). Moreover, the Cu clusters were in average dimeter of ~0.91 nm possessing ~9 copper atoms (Figs. 5b and S2). The elemental mapping confirmed a uniform distribution of Cu elements (Fig. 5c–f).

3.2.2.3. XAFS analysis. The XANES of Cu/CNS-spent and Cu/NCNS-spent showed similar edge shapes for CuO reference (Fig. 6a), indicating the oxidized Cu species, agreeing with the XRD results. Besides, a distinct peak at ~1.50 Å and a weak peak at ~2.1 Å (without phase correction) were observed in the EXAFS spectra of all spent catalysts (Fig. 6b). The weak peak at ~2.1 Å were attributed to Cu-Cu bonds. The distinct peak at ~1.50 Å, could match up with the Cu-C/O on Cu/CNS-spent and Cu-C/N bonds on Cu/NCNS-spent, respectively, due to the fact that Cu-C, Cu-O and Cu-N bond is difficult to distinguish in EXAFS [35]. This result indicated that Cu clusters were located on support through Cu-C or Cu-N bonds. Given the above results, it is strongly suggested that the reconstruction of Cu NPs occurred during the reaction, and large Cu NPs (~11 nm) were redispersed into small clusters as well as single-atom sites that were incorporated into nanosheets. From the above analysis, we could come to a very different conclusion from previous studies, that is, no aggregation of copper species occurred after

the reaction, whereas a substitute reconstruction procedure of active species was highly recommended.

3.2.2.4. N-XPS and TPR. As can be seen from the N 1s spectra of the fresh catalysts (Fig. 7a), pyridinic (N_{pd}), pyrrolic (N_{pr}), graphitic (N_g) and oxidized N (N_{ox}) species at 398.2, 398.9, 401.3 and 405.0 eV were observed, respectively. With increasing N-doping content, the surface total N concentration, especially the concentration of (N_{pd} + N_g), serving as effective anchoring sites for metal NPs, increased from 39.5% to 56.7% (Table 4), which can be regarded as the main cause of the increase of Cu dispersion in the fresh catalysts [36,37]. A slight decrease of Cu dispersion on Cu/NCNS-12 compared with Cu/NCNS-8 was likely to result from the excessive N content [38]. Noticeably, a new peak belonging to the N–Cu bond (~399.0 eV) appeared in the N 1s XPS spectra of the spent catalysts (Fig. 7b), providing further evidence for the presence of the Cu-N coordination interaction, which indicated the occurrence of the enhanced metal-support interaction because of the reconstruction of Cu species [39]. The finding was also confirmed by the TPR of the spent catalysts (Fig. 8), in which the reduction peak of copper species shifted toward higher temperature.

3.2.3. Chemical states of copper

3.2.3.1. Cu-XPS, TPR and CH_3OH-TPD. As shown in Fig. 9a, the Cu 2p XPS spectra of the fresh catalysts showed only two peaks centered at 932.5 and 952.5 eV, assigned to Cu^+ and Cu^0 species. The absence of the Cu 2p satellite peak at 940–946 eV indicated that the surface Cu^{2+} species had been completely reduced to a lower valence state, in accordance with the XRD result. Comparing with the Cu/CNS, the Cu 2p peak of Cu/NCNS gradually shifted to low BE with the increase in N-doping content, indicative of the enhanced metal-support interaction caused by the electron-donating effects of N species [6], which was confirmed by the shift of reduction peaks to a higher temperature for the fresh catalysts (Fig. 8). The Cu^+ and Cu^0 species were distinguished by deconvoluting the two overlapping peaks at 912.5 and 916.5 eV [15, 40], respectively, in the Cu LMM spectra (Fig. 9b), and the detailed

Table 3
Practical Cu loading and surface Cu species analysis of Cu/CNS and Cu/NCNS catalysts.

Catalysts	Cu[a] (wt%)		Cu[b] (at%)		$X_{Cu}{}^{2+}$ (%)[c]		$X_{Cu}{}^+$ (%)[d]		$X_{Cu}{}^0$ (%)[e]		Cu^0 (at%)[f]	
	Fresh	Spent	Fresh	Spent	Fresh	Spent	Fresh	Spent	Fresh	Spent	Fresh	Spent
Cu/CNS	10.6	8.5	0.81	2.98	0	86.5	41.3	6.1	58.7	7.4	0.48	0.22
Cu/NCNS-4	10.5	8.5	1.06	2.69	0	78.6	36.4	9.4	63.6	12.0	0.67	0.32
Cu/NCNS-8	10.3	8.8	1.47	1.91	0	62.5	35.7	14.6	64.3	22.9	0.95	0.44
Cu/NCNS-12	10.6	8.6	1.30	2.29	0	53.2	35.5	16.2	64.5	30.6	0.84	0.70

[a] Determined by AAS.
[b] Determined by XPS.
[c] $Cu^{2+}/(Cu^{2+} + Cu^+ + Cu^0)$ calculated from Cu 2p deconvolution result.
[d] $Cu^+/(Cu^{2+} + Cu^+ + Cu^0)$ calculated from 100* $(Cu^0 + Cu^+)$ (%, from the deconvolution result of Cu 2p) * Cu^+ (%, from the deconvolution result of Cu LMM).
[e] $Cu^0/(Cu^{2+} + Cu^+ + Cu^0)$ calculated from 100* $(Cu^0 + Cu^+)$ (%, from the deconvolution result of Cu 2p) * Cu^0 (%, from the deconvolution result of Cu LMM).
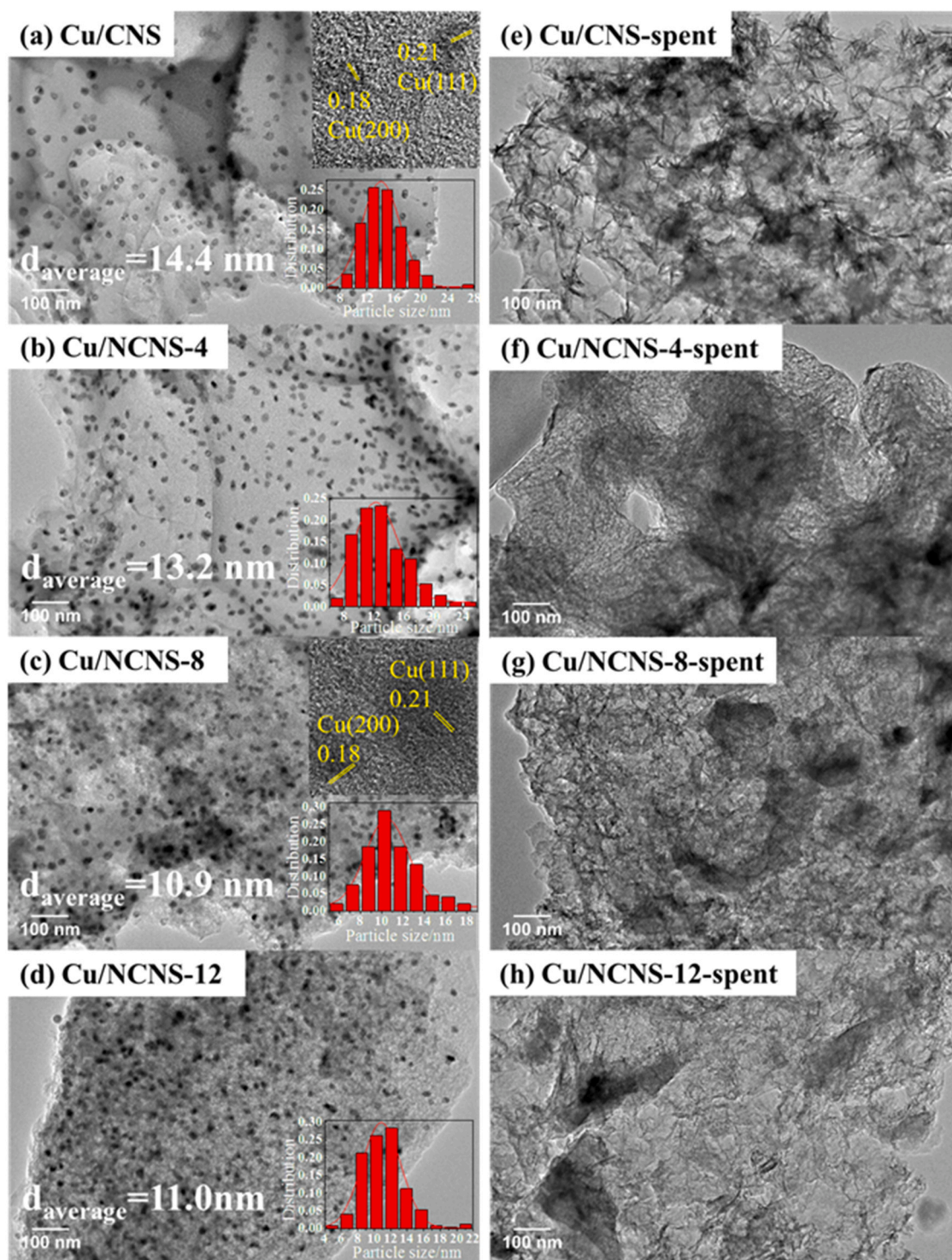[f] Cu^0 calculated from Cu[b] * $X_{Cu}{}^{0e}$.

Fig. 3. TEM images of (a–d) the fresh and (e–h) spent Cu/CNS and Cu/NCNS catalysts.

analysis results are shown in Table 3. It was noted that the X_{Cu}^0 value linearly increased with the increase in the surface total nitrogen concentration (Fig. 9c). The surface Cu^0 concentration of Cu/NCNS first increased and then decreased with increasing surface N-doping content, and reached the maximum (0.95 at%) on the Cu/NCNS-8 catalyst (Table 3), in agreement with the TEM observation. This finding implied that the introduction of nitrogen in CNS promoted the formation of Cu^0 species. In addition, it was found that the adsorption amount of CH_3OH reached the maximum value on the Cu/NCNS-8 catalyst (Fig. S3), verifying the presence of the most active sites among all of the catalysts.

3.2.3.2. Cu-XPS analysis. In the case of spent catalysts, an additional peak emerging at 934.6 eV accompanied by a satellite at 939–946 eV was observed (Fig. 9d), manifesting the formation of CuO species, in line with the XRD result (Fig. 4b). It can be concluded that CuO, Cu_2O and Cu^0 coexisted in all of the spent catalysts. Notably, the peak of Cu^0 (Fig. 9e) was steadily shifted to lower BE with increasing surface N-doping content (up to 0.6 eV), which provided definite evidence of the enhanced interaction between Cu^0 and nitrogen species for optimizing the electronic structures of Cu clusters [41]. As can be seen from Table 3, the X_{Cu}^0 decreased for all the catalysts after the reaction, and the drop
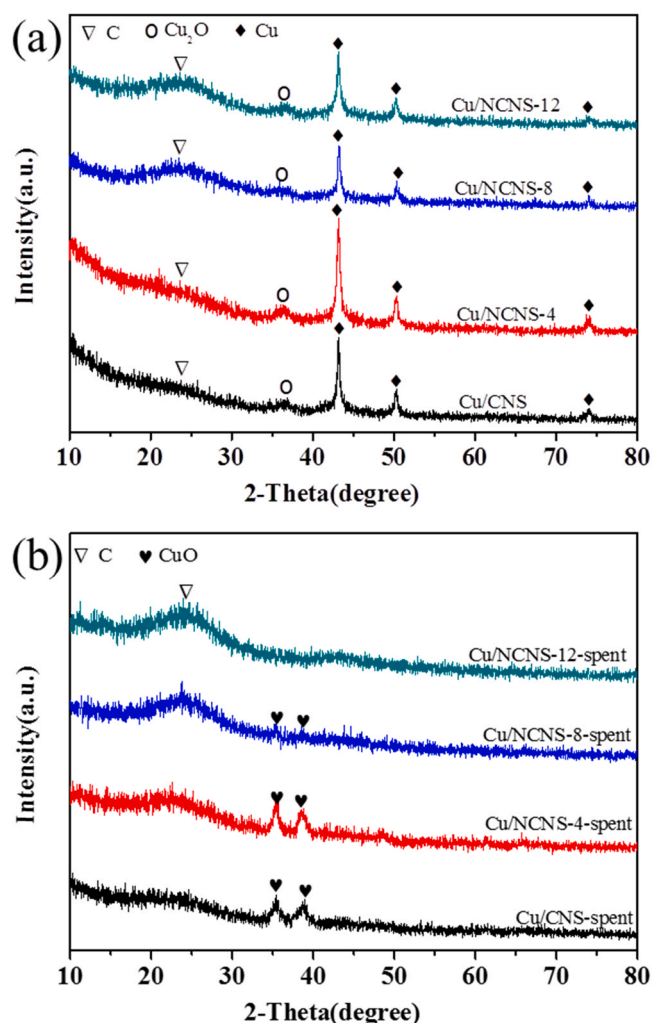
Fig. 4. XRD patterns of (a) the fresh and (b) spent Cu/CNS and Cu/NCNS catalysts.

rate of X_{Cu}^0 linearly decreased with increasing surface nitrogen concentration (Fig. 9f). Accordingly, the surface Cu^0 concentration in the spent catalysts increased gradually and achieved the maximum of 0.70 at% for the Cu/NCNS-12-spent. Therefore, it can be concluded that the resistance to oxidation of Cu^0 species was significantly enhanced in the oxidative carbonylation reaction. Based on the above results, it was clear that the introduction of nitrogen in the CNS could efficiently promote the formation of Cu^0 in the fresh catalysts, as well as enhance the stability of active Cu^0 species in the Cu/NCNS catalysts during the reaction process [15,29,37].

4. Discussion

4.1. Structure-activity relationship

Fig. 1 shows that Cu/NCNS exhibited far better activity and stability than the Cu/CNS catalyst. With increasing N-doping content, the initial activity first increased and then decreased, reaching the maximum for the Cu/NCNS-8, while the stability of the Cu/NCNS catalysts increased steadily. As reported in our previous work, the experimental and theoretical investigations showed the sequence of the catalytic activity of Cu species in this reaction was $CuO < Cu_2O < Cu^0$, and Cu^0 was the best catalytic active center [42–44]. Furthermore, the reaction mechanism over Cu^0 supported on carbon catalysts was revealed via the theoretical calculation [15,45]. As shown in Fig. S4, the path 1 was the main

pathway for DMC formation, and the insertion of CO into methoxide (R2) was the rate-determining step. Moreover, the number of exposed Cu^0 species was found to be critical for the catalytic properties of carbon-supported copper catalysts [15,45]. As shown in Table 3, the variation in initial activity in these catalysts was consistent with their surface Cu^0 concentration. Besides, the Cu/NCNS-8 possessed a higher BET specific area as well as a higher larger pore volume, indicative of well-developed interconnection of pores, which could promote the accessibility of active sites to reactants and further endow an enhanced catalytic performance [2,32].

In addition, it is known that the leaching, aggregation and oxidation of Cu^0 active species frequently lead to deactivation of copper supported on a carbon catalyst in DMC synthesis [12,14]. In this work, the Cu reconstruction occurred with a slight leaching for both Cu/CNS and Cu/NCNS catalysts. Moreover, it is evident that the fully exposed Cu clusters, compared with single-atom Cu sites, can exhibit better catalytic performance due to their designated metallic valence states with multiple metal atoms and a full atomic utilization efficiency [46–50]. Finally, the oxidation of Cu^0 species was efficiently inhibited with enhanced metal–support interaction caused by the introduced N species. The high N-doped Cu/NCNS catalyst, therefore, exhibited excellent activity and stability in DMC synthesis.

4.2. Insight into the reconstruction of copper species

In this study, apart from the improved anti-leaching and anti-aggregation effects, the most interesting feature was that the reconstruction of Cu NPs occurred during the reaction process. More recently, the reconstruction of metal catalysts, including size and morphology changes, composition evolution, surface reconstruction of metal oxides support, and strong metal-support interactions, have aroused tremendous interest [51–54]. Among various types of reconstruction phenomena, it has been found that the reconstruction of metal NPs, containing noble metal (Pt, Pd and Rh) and transition metal (Fe, Mo and Ni), could efficiently prevent catalyst deactivation in a variety of reactions [55–58]. In particular, Jan and Xu reported that the reconstruction of Cu species under reaction process resulted in the high electrocatalytic performance in CO_2 reduction reaction (CO_2RR) [59, 60]. It has been argued that sintering and reconstruction are two sides of the same process, which is mainly influenced by temperature, pressure, gas environment, structure of catalyst and so on [56,61–62].

According to the results obtained above, the Cu reconstruction occurred in all cases, irrespective of N-doping in these catalysts. To illustrate the origin of the reconstruction, we further investigated the effect of different operating conditions on the Cu reconstruction for the Cu/NCNS-12 catalyst. Notably, all the investigations were based on the presence of solvent. The TEM images after 1 run are shown in Fig. S5, and the detailed experimental conditions are given in Table S2. No metal NPs were detected in the Cu/NCNS-12-spent catalyst under different atmospheres of $CO + O_2$, $O_2 + N_2$, $CO + N_2$ and N_2 (Fig. S5a–d), different solvents (H_2O and *n*-hexane) (Fig. S5e and f), low rotation speed as well as low pressure (Fig. S5g and h), suggesting a lack of influence of these operation conditions on the reconstruction process. However, as the temperature was lowered to 90 °C (Fig. S5i–k), obvious Cu NPs (9.6 nm) could be observed, and further decreasing the temperature to 80 °C led to a serious agglomeration of Cu NPs (~40.0 nm) (Fig. S5l). Meanwhile, the Cu concentration was 8.7 wt% after 1 run (Table S3), which was nearly identical to that of 10 runs (8.6 wt%). Furthermore, no metal NPs could be observed after 3 and 10 runs (Figs. S6 and 3h). In comparison with the AAS and TEM results after 1 run and 10 runs, it was clear that the Cu reconstruction occurred after the first run and the reconstructed clusters was a high aggregation and leaching resistance during the subsequent nine runs.

Surprisingly, we can conclude that the temperature was the only key factor to drive reconstruction of Cu NPs, which was likely to be related to the carbon defects [58]. According to the literature, carbon material
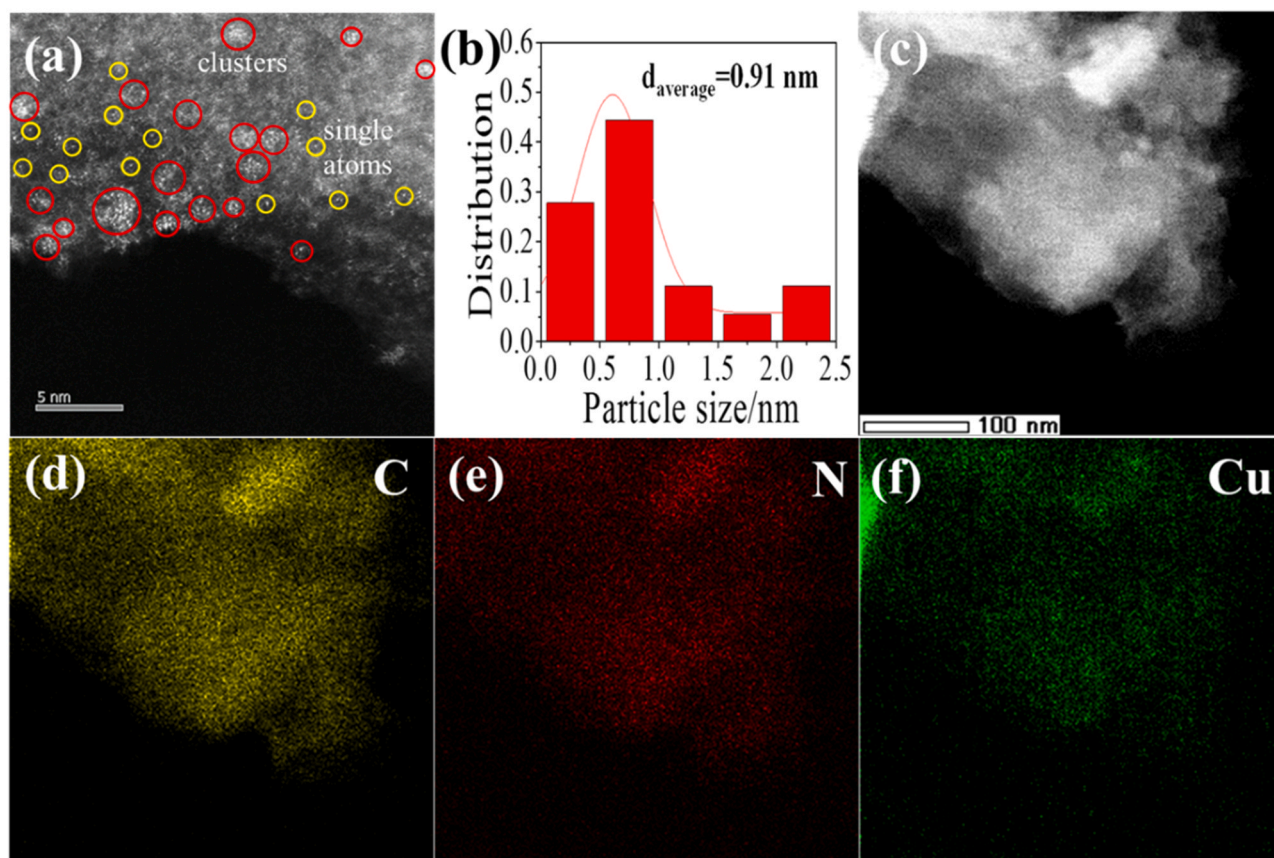
Fig. 5. (a) HAADF-STEM, (b) corresponding size distribution, and (c-f) elemental mapping images of the spent Cu/NCNS-12 catalyst.
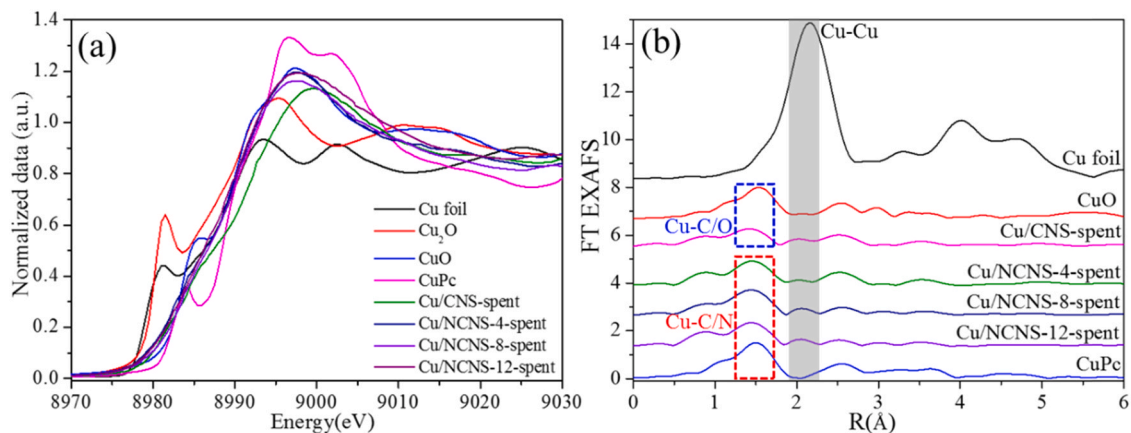

Fig. 6. (a) Cu K-edge XANES spectra of the Cu/CNS-spent and Cu/NCNS-12-spent catalysts and reference samples (Cu foil, Cu_2O, CuO and CuPc) and (b) Fourier transform extend X-ray absorption fine structure spectra (FT-EXAFS) in the R space of Cu/CNS-spent and Cu/NCNS-12-spent.

itself is a defect-rich support including plane topological defect sites, edge defects, vacancy defects and carbon defects coupled with hetero-atom doping sites [63,64]. Both the experimental and theoretical results showed that these defects could serve as effective defective sites to stabilize the metal particles, clusters and single atoms [65,66], and more defects can be fabricated at high temperatures [58]. Here, Raman measurement was employed to detect carbon defects. The I_D/I_G value of these four catalysts was similar before and after reaction (Fig. 10), which suggested that no more defects were detected on the spent sample. Similarly, the I_D/I_G value of bare support also showed negligible change before and after reaction (Fig. S7). Furthermore, a comparison of the Raman spectra of Cu/NCNS-12 catalyst with that of NCNS-12 clearly

showed a decreased I_D/I_G value for Cu-loaded samples, indicating the formation of Cu NPs or clusters at the defective sites to lower the carbon defect density after Cu loading [65]. Based on above result, it can be inferred that new carbon defects were dynamically activated at high temperature ($\geq$100 °C) [58,67–68], and the initial large-sized Cu NPs migrated, and then were trapped into newly created defect sites, finally forming small clusters along with individual single atoms and strongly incorporated into the defects on the CNS support. Meanwhile, it is the chemical confinement of carbon defects originating from the support that efficiently prevented the Cu leaching as mentioned above [20,69].

Furthermore, DFT calculations were performed to further illustrate the crucial role of carbon defects in the formation and stabilization of Cu
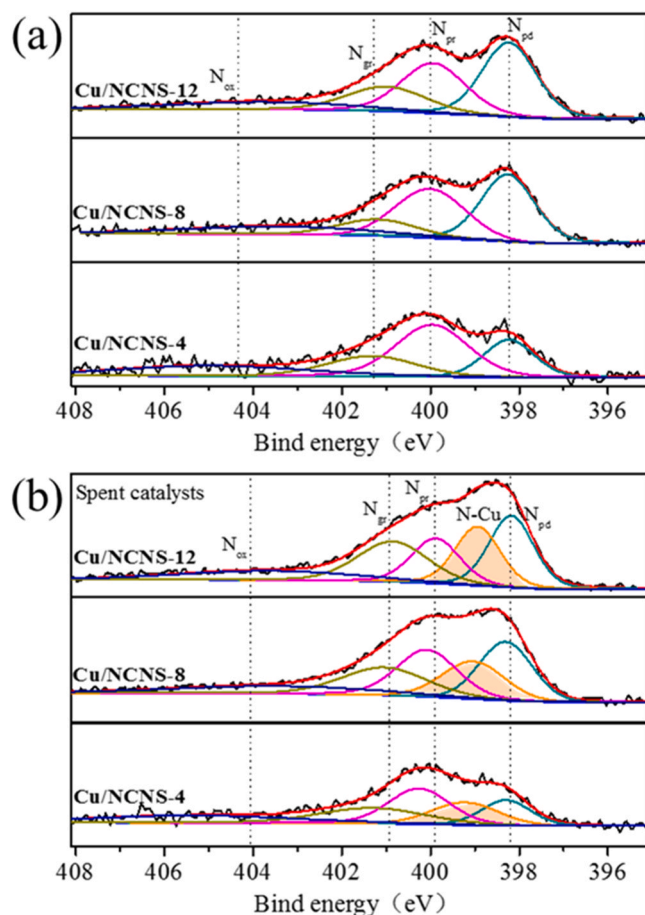
Fig. 7. N_{1s} XPS spectra of (a) the fresh and (b) spent Cu/NCNS catalysts.

previously, which were fabricated at 500 °C in a H_2 atmosphere [58]. Therefore, this work showed clear advantages in the preparation of carbon-supported metal catalysts with facile operation conditions as well as higher loading levels of metal clusters or metal single atoms.

4.3. The superior anti-oxidation effect induced by nitrogen species

Apart from the leaching and aggregation of Cu NPs, oxidation of the main active Cu^0 species is considered as another deactivation factor. Hence, improving the oxidation resistance can be a key attempt to improve the stability of carbon-supported copper catalysts. Especially, the difference in catalytic stability are thought to arise from the difference in the anti-oxidation ability of Cu^0 species in the Cu/CNS and Cu/NCNS catalysts after Cu reconstruction.

As mentioned previously, in addition to metal size effect, the introduction of nitrogen species in a carbon support can regulate the electronic state of the metal species, thereby improving the anti-oxidation ability [37]. Wang and co-workers used a theoretical investigation to show that incorporating N species increased the proportion of Pt^0 via the enhanced Pt–support interaction, and the stronger interaction prevented the oxidation of Pt^0 in air [37]. Xia and co-workers experimentally confirmed that the surface N species on carbon nanotubes promoted the formation of Co^0 species, and improved the resistance of Co^0 species against oxidation in ambient atmosphere because of the electronic interaction between Co and N-doped support [29].

In the present work, XPS results showed that the introduced N species, as electron donor, optimized the electronic structure of Cu species. For fresh catalysts, the Cu/NCNS showed a higher proportions of Cu^0 than Cu/CNS, confirming the incorporation of N species is in favor of the formation of metallic state species, in agreement with reports [37]. Meanwhile, the N species increased the electronic density of Cu^0 species via electron transfer from N species to the Cu^0 center, indicating the enhanced interaction between Cu^0 and NCNS (Fig. 9a and e). The
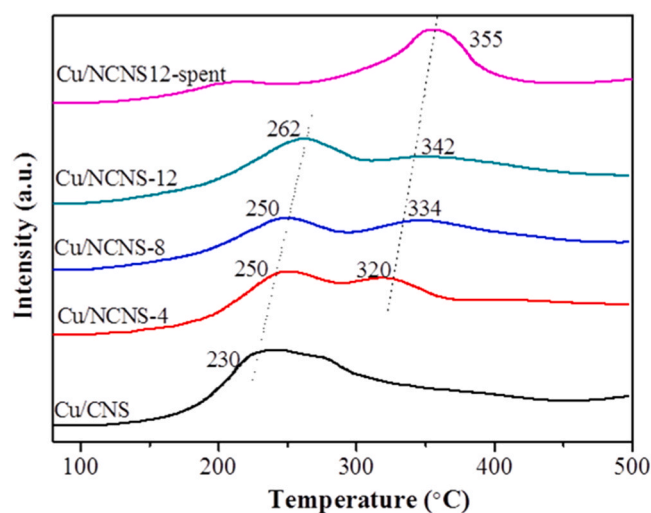
clusters. The Cu clusters supported carbon models included perfect carbon (Cu_8/PC) and Cu_8/defect carbon (Cu_8/DC) models (vacancy DC (Cu_8/DC_v), N-doped defect carbon with low nitrogen content (Cu_8/N_lC) and N-doped defect carbon with high nitrogen content (Cu_8/N_hC)) (Fig. 11a and b). Fig. 11c clearly shows that the adsorbing energy of Cu_8 clusters on the DC are higher than that of Cu_8/PC, irrespective of the type of defects and the concentration of N species. This phenomenon indicated a relatively strong interaction between Cu clusters and carbon defects in the DC structures, and thus, Cu clusters can be formed and stabilized by the defects.

Interestingly, it is previously reported that the dynamic reconstruction of Cu occurred with the change of voltage under the reaction conditions, and was strongly dependent on the CO_2RR reaction [59,60]. In the present study, the Cu reconstruction was found to be initiated at a relative milder condition. Moreover, the Cu loading of the Cu/NCN and Cu/NCNS catalysts (~10.0 wt%) was higher than that of Cu clusters or Cu single atoms supported on carbon materials (≤ 5.0 wt%), including defect-rich carbon derived from litchi pericarp and XC-72 carbon [60, 69]. It is noted that the activation temperature of carbon defects on the CNS and NCNS was far lower than that on carbon cloth reported

Fig. 8. H_2-TPR profiles of the fresh Cu/CNS, Cu/NCNS and the spent Cu/NCNS-12 catalysts.

Table 4
Surface N species analysis of Cu/NCNS catalysts.

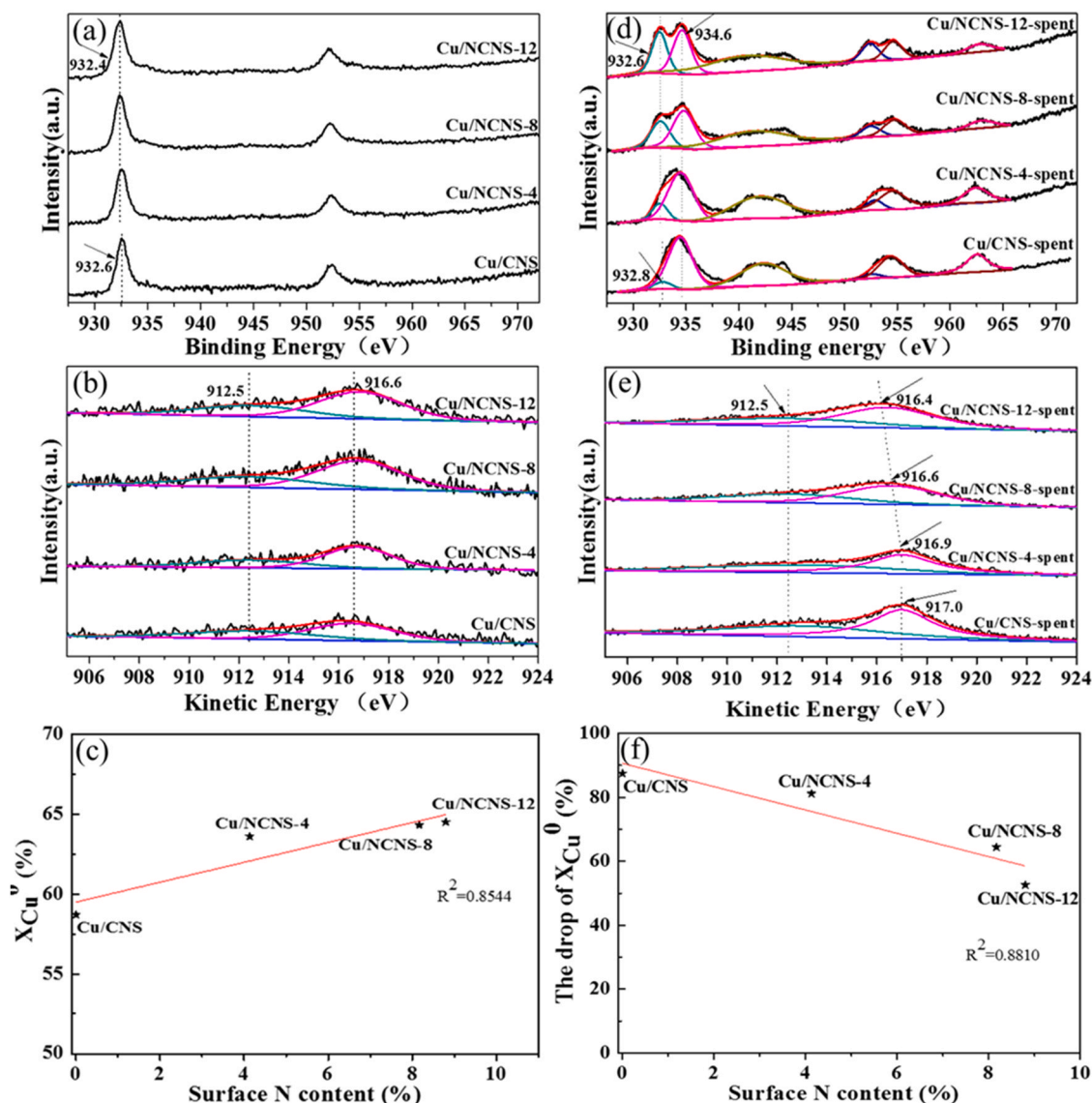| Sample	N (at%)[a]	N_{pd} (%)		N-Cu (%)		N_{pr} (%)		N_g (%)		N_{ox} (%)	
	Fresh	Fresh	Spent	Fresh	Spent	Fresh	Spent	Fresh	Spent	Fresh	Spent
Cu/NCNS-4	4.13	20.1	15.4	0	18.1	40.0	27.2	19.4	20.9	20.5	18.4
Cu/NCNS-8	8.17	37.4	24.5	0	18.6	32.5	23.9	13.5	19.9	16.6	13.1
Cu/NCNS-12	8.80	38.1	25.8	0	21.6	30.4	17.7	18.6	22.9	12.9	12.0

[a] Determined by XPS.

Fig. 9. (a) Cu $2p_{3/2}$ XPS and (b) Cu LMM Auger spectra of the fresh Cu/CNS and Cu/NCNS catalysts, (c) relationship between X_{Cu}^0 and the surface N concentration, (d) Cu $2p_{3/2}$ XPS and (e) Cu LMM Auger spectra of the spent catalysts, (f) relationship between the drop of X_{Cu}^0 and the surface N concentration.
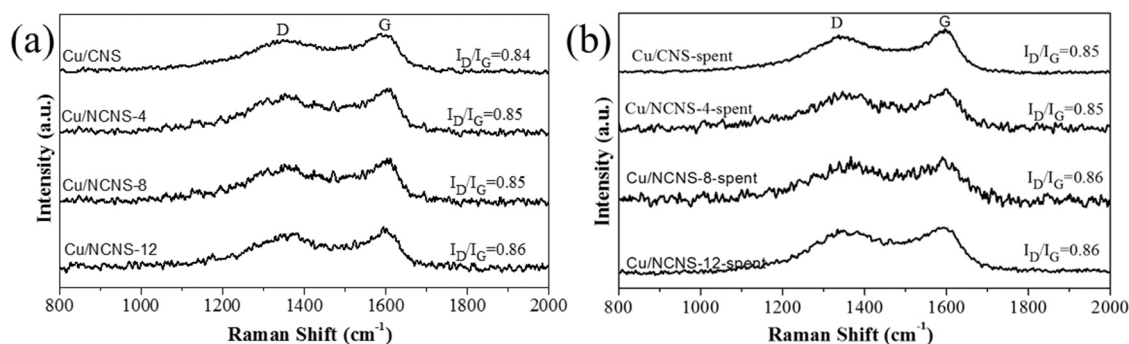

Fig. 10. Raman spectra of (a) fresh and (b) spent Cu/CNS and Cu/NCNS catalysts.

presence of strong interaction greatly inhibited the oxidation of Cu^0 during the reaction process. Particularly, the correlation between surface N concentration and the antioxidant capacity of Cu^0 was further established, which was rarely reported. The anti-oxidation of Cu^0 species linearly increased with increasing surface N concentration and

reached the maximum on the Cu/NCNS-12 catalyst (Fig. 9f). This result indicated the extremely significant effect of a high N content to anti-oxidation of metallic copper species.

From the analysis above, it was concluded that the significantly improved catalytic performance of Cu/NCNS was ascribed to the
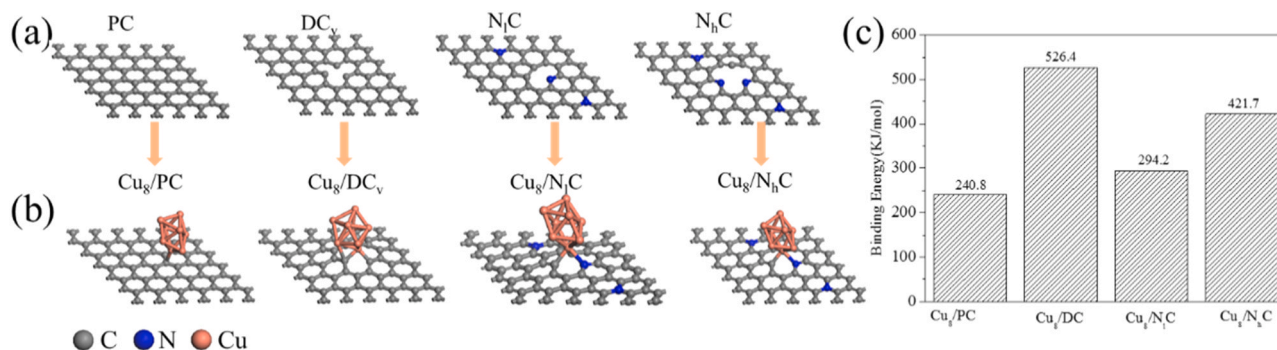
Fig. 11. DFT calculations with the models of (a) PC, DC_v, N_lC and N_hC, (b) corresponding models after the deposition of Cu_8 clusters, and (c) the adsorbing energy of Cu_8 clusters on the support.

synergistic effect between the hierarchical porous structure of nanosheets and the introduced N species. The hierarchical porous nanosheets structure not only maximized the exposure of active Cu sites but also provided new defects to result in the reconstruction of Cu, while the strong interaction between Cu^0 and N atoms strongly prevented the oxidation of Cu^0 species.

5. Conclusion

In summary, a series of Cu/NCNS catalysts containing different N content was prepared and exhibited excellent activity and stability compared with Cu/CNS in the oxidative carbonylation of methanol. The cycling stability was observed to be gradually increased with increasing N-doping content in the Cu/NCNS catalysts. The improved catalytic performance could be ascribed to the synergistic effect between the hierarchical porous structure of CNS as well as the introduction of N species in the carbon framework. The porous nanosheets provided new carbon defects to reconstruct the original Cu NPs (~11 nm) into small clusters (~0.91 nm) along with individual single atoms during the reaction process, which efficiently restrained the leaching and aggregation of copper species. Further investigation showed that the reconstruction was merely driven at a temperature higher than 100 °C, regardless of atmosphere, solvent types, pressure as well as rotation speed. In addition, the introduced N species favored the formation and stabilization of Cu^0 species, attributed to the strong interaction between Cu^0 and N atoms. The optimal Cu/NCNS-12 catalyst exhibited no obvious activity decay even after 10 recycling runs, far higher than those of previous carbon-supported copper catalysts. This work highlighted the importance of the NCNS on the design of the copper-supported catalyst with superior performance against leaching, aggregation and oxidation, and thus provides a new way for the targeted development of high performance catalysts.

CRediT authorship contribution statement

Yongli Pei: Conceptualization, Methodology, Formal analysis, Investigation, Data curation, Writing – original draft, Writing – review & editing. **Yanhong Quan:** Formal analysis, Investigation, Writing – review & editing. **Xuhui Wang:** performing the DFT calculations. **Jinxian Zhao:** Investigation, Formal analysis. **Ruina Shi:** Investigation, Formal analysis. **Zhong Li:** Investigation, Formal analysis. **Jun Ren:** Writing – review & editing, Supervision.

Declaration of Competing Interest

The authors declare no conflict of interest.

Appendix A. Supporting information

Supplementary data associated with this article can be found in the online version at doi:10.1016/j.apcatb.2021.120718.

References

[1] M. Tang, J. Deng, M. Li, X. Li, H. Li, Z. Chen, Y. Wang, 3D-interconnected hierarchical porous N-doped carbon supported ruthenium nanoparticles as an efficient catalyst for toluene and quinoline hydrogenation, Green Chem. 18 (2016) 6082–6090.
[2] M. Li, J. Deng, Y. Lan, Y. Wang, Efficient catalytic hydrodeoxygenation of aromatic carbonyls over a nitrogen-doped hierarchical porous carbon supported nickel catalyst, ChemistrySelect 2 (2017) 8486–8492.
[3] H. Su, P. Gao, M. Wang, G. Zhai, J. Zhang, T. Zhao, J. Su, M. Antonietti, X. Li, J. Chen, Grouping effect of single nickel−N_4 Sites in nitrogen-doped carbon boosts hydrogen transfer coupling of alcohols and amines, Angew. Chem. 57 (2018) 15194–15198.
[4] S. Iqbal, S.A. Kondrat, D.R. Jones, D.C. Schoenmakers, J.K. Edwards, L. Lu, B. R. Yeo, P.P. Wells, E.K. Gibson, D.J. Morgan, C.J. Kiely, G.J. Hutchings, Ruthenium nanoparticles supported on carbon: an active catalyst for the hydrogenation of lactic acid to 1,2-propanediol, ACS Catal. 5 (2015) 5047–5059.
[5] Y. Cao, M. Tang, M. Li, J. Deng, F. Xu, L. Xie, Y. Wang, In situ synthesis of chitin-derived Rh/N−C cataylsts: efficient hydrogenation of benzoic acid and derivatives, ACS Sustain. Chem. Eng. 5 (2017) 9894–9902.
[6] Z. Wei, X. Li, J. Deng, J. Wang, H. Li, Y. Wang, Improved catalytic activity and stability for hydrogenation of levulinic acid by Ru/N-doped hierarchically porous carbon, Mol. Catal. 448 (2018) 100–107.
[7] H. Tan, Z. Wang, Z. Xu, J. Sun, Y. Xu, Q. Chen, Y. Chen, G. Guo, Review on the synthesis of dimethyl carbonate, Catal. Today 316 (2018) 2–12.
[8] S. Huang, B. Yan, S. Wang, X. Ma, Recent advances in dialkyl carbonates synthesis and applications, Chem. Soc. Rev. 44 (2015) 3079–3116.
[9] G. Zhang, Z. Li, H. Zheng, T. Fu, Y. Ju, Y. Wang, Influence of the surface oxygenated groups of activated carbon on preparation of a nano Cu/AC catalyst and heterogeneous catalysis in the oxidative carbonylation of methanol, Appl. Catal. B Environ. 179 (2015) 95–105.
[10] R. Shi, J. Wang, J. Zhao, S. Liu, P. Hao, Z. Li, J. Ren, Cu nanoparticles encapsulated with hollow carbon spheres for methanol oxidative carbonylation: Tuning of the catalytic properties by particle size control, Appl. Surf. Sci. 459 (2018) 707–715.
[11] G. Zhang, D. Zhao, J. Yan, D. Jia, H. Zheng, J. Mi, Z. Li, The promotion and stabilization effects of surface nitrogen containing groups of CNT on Cu-based nanoparticles in the oxidative carbonylation reaction, Appl. Catal. A Gen. 579 (2019) 18–29.
[12] J. Zhao, R. Shi, Y. Quan, J. Liu, J. Wang, Y. Pei, X. Wang, Z. Li, J. Ren, Highly efficient synthesis of dimethyl carbonate over copper catalysts supported on resin-derived carbon microspheres, Chem. Eng. Sci. 207 (2019) 1060–1071.
[13] P. Hao, J. Ren, L. Yang, Z. Qin, J. Lin, Z. Li, Direct and generalized synthesis of carbon-based yolk-shell nanocomposites from metal-oleate precursor, Chem. Eng. J. 283 (2016) 1295–1304.
[14] J. Ren, P. Hao, R. Sun Wei, S. Shi, Liu, Ordered mesoporous silica-carbon-supported copper catalyst as an efficient and stable catalyst for catalytic oxidative carbonylation, Chem. Eng. J. 328 (2017) 673–682.

[15] R. Shi, J. Zhao, S. Liu, W. Sun, H. Li, P. Hao, Z. Li, J. Ren, Nitrogen-doped graphene supported copper catalysts for methanol oxidative carbonylation: Enhancement of catalytic activity and stability by nitrogen species, Carbon 130 (2018) 185–195.

[16] K.S. Novoselov, A. Mishchenko, A. Carvalho, A.H. Castro Neto, 2D materials and van der Waals heterostructures, Science 353 (2016) aac9439–1–11.

[17] Z. Sun, T. Ma, H. Tao, Q. Fan, B. Han, Fundamentals and challenges of electrochemical CO_2 reduction using two-dimensional materials, Chem 3 (2017) 560–587.

[18] S. Li, J. Gong, Strategies for improving the performance and stability of Ni-based catalysts for reforming reactions, Chem. Soc. Rev. 43 (2014) 7245–7256.

[19] X. Huang, F. Guo, M. Li, H. Ren, Y. Shi, L. Chen, Hydrothermal synthesis of $ZnSnO_3$ nanoparticles decorated on g-C_3N_4 nanosheets for accelerated photocatalytic degradation of tetracycline under the visible-light irradiation, Sep. Purif. Technol. 230 (2020) 1–8.

[20] Z. Chen, W. Wang, Y. Zhang, Y. Liang, Z. Cui, X. Wang, Pd nanoparticles confined in the porous graphene-like carbon nanosheets for olefin hydrogenation, Langmuir 34 (2018) 12809–12814.

[21] C. Lin, G. Wu, H. Li, Y. Geng, G. Xie, J. Yang, B. Liu, J. Jin, Rh nanoparticles supported on ultrathin carbon nanosheets for high-performance oxygen reduction reaction and catalytic hydrogenation, Nanoscale 9 (2017) 1834–1839.

[22] Q. Wang, L. Wang, Z. Tang, F. Wang, W. Yan, H. Yang, W. Zhou, L. Li, X. Kang, S. Chen, Oxygen reduction catalyzed by gold nanoclusters supported on carbon nanosheets, Nanoscale 8 (2016) 6629–6635.

[23] G. Sun, L. Zhou, J. Li, J. Tang, Y. Wang, Human hair-derived graphene-like carbon nanosheets to support Pt nanoparticles for direct methanol fuel cell application, RSC Adv. 5 (2015) 71980–71987.

[24] X. Zhang, Z. Wei, Q. Guo, H. Tian, Kinetics of sodium borohydride hydrolysis catalyzed via carbon nanosheets supported Zr/Co, J. Power Sources 231 (2013) 190–196.

[25] P. Zuo, J. Duan, H. Fan, S. Qu, W. Shen, Facile synthesis high nitrogen-doped porous carbon nanosheet from pomelo peel and as catalyst support for nitrobenzene hydrogenation, Appl. Surf. Sci. 435 (2018) 1020–1028.

[26] F. Zhong, Q. Wang, C. Xu, Y. Yang, Y. Wang, Y. Zhang, D. Gao, J. Bi, G. Fan, Ultrafine and highly dispersed Ru nanoparticles supported on nitrogen-doped carbon nanosheets: efficient catalysts for ammonia borane hydrolysis, Appl. Surf. Sci. 455 (2018) 326–332.

[27] Y. Liu, X. Xu, P. Sun, T. Chen, N-doped porous carbon nanosheets with embedded iron carbide nanoparticles for oxygen reduction reaction in acidic media, Int. J. Hydrog. Energy 40 (2015) 4531–4539.

[28] B. Zhang, J. Zhang, X. Tao, Q. Mei, L. Zheng, Ultrathin and porous carbon nanosheets supporting bimetallic nanoparticles for high-performance electrocatalysis, ChemCatChem 10 (2018) 1241–1247.

[29] P. Chen, F. Yang, A. Kostka, W. Xia, Interaction of cobalt nanoparticles with oxygen- and nitrogen- functionalized carbon nanotubes and impact on nitrobenzene hydrogenation catalysis, ACS Catal. 4 (2014) 1478–1486.

[30] X. Yu, J. Zhao, R. Lv, Q. Liang, C. Zhan, Y. Bai, Z.H. Huang, W. Shen, F. Kang, Facile synthesis of nitrogen-doped carbon nanosheets with hierarchical porosity for high performance supercapacitors and lithium-sulfur batteries, J. Mater. Chem. A 3 (2015) 18400–18405.

[31] C.J.G. Van Der Grift, A.F.H. Wielers, B.P.J. Jogh, J. Van Beunum, M. De Boer, M. Versluijs-Helder, J.W. Geus, Effect of the reduction treatment on the structure and reactivity of silica-supported copper particles, J. Catal. 131 (1991) 178–189.

[32] Y. Pei, J. Zhao, R. Shi, X. Wang, Z. Li, J. Ren, Hierarchical porous carbon-supported copper nanoparticles as an efficient catalyst for the dimethyl carbonate synthesis, Catal. Lett. 149 (2019) 3184–3193.

[33] Y. Yuan, W. Cao, W. Weng, $CuCl_2$ immobilized on amino-functionalized MCM-41 and MCM-48 and their catalytic performance toward the vapor-phase oxy-carbonylation of methanol to dimethylcarbonate, J. Catal. 228 (2004) 311–320.

[34] A.T. Bell, The impact of nanoscience on heterogeneous catalysis, Science 299 (2003) 1688–1691.

[35] X. Chen, M. Peng, X. Cai, B. Mei, Z. Jiang, D. Xiao, Y. Chen, Z. Jia, Y. Deng, X. Wen, N. Wang, H. Liu, Regulating coordination number in atomically dispersed Pt species on defect-rich graphene for n-butane dehydrogenation reaction, Nat. Commun. (2021) 1–9.

[36] H. Li, J. Zhao, R. Shi, P. Hao, S. Liu, Z. Li, J. Ren, Remarkable activity of nitrogen-doped hollow carbon spheres encapsulated Cu on synthesis of dimethyl carbonate: role of effective nitrogen, Appl. Surf. Sci. 436 (2018) 803–813.

[37] Y. Cao, S. Mao, M. Li, Y. Chen, Y. Wang, Metal/porous carbon composites for heterogeneous catalysis: old catalysts with improved performance promoted by N-doping, ACS Catal. 7 (2017) 8090–8112.

[38] Y. Jiang, X. Fan, M. Chen, X. Xiao, Y. Zhang, C. Wang, L. Chen, AuPd nanoparticles anchored on nitrogen-decorated carbon nanosheets with highly efficient and selective catalysis for the dehydrogenation of formic acid, J. Phys. Chem. C 122 (2018) 4792–4801.

[39] D.A. Bulushev, A.L. Chuvilin, V.I. Sobolev, S.G. Stolyarova, Y.V. Shubin, I. P. Asanov, A.V. Ishchenko, G. Magnani, M. Riccò, A.V. Okotrub, L.G. Bulusheva, Copper on carbon materials: stabilization by nitrogen doping, J. Mater. Chem. A 5 (2017) 10574–10583.

[40] Y. Zhao, Z. Guo, H. Zhang, B. Peng, Y. Xu, Y. Wang, J. Zhang, Y. Xu, S. Wang, X. Ma, Hydrogenation of diesters on copper catalyst anchored on ordered hierarchical porous silica: pore size effect, J. Catal. 357 (2018) 223–237.

[41] Q. Hu, Z. Han, X. Wang, G. Li, Z. Wang, X. Huang, H. Yang, X. Ren, Q. Zhang, J. Liu, C. He, Facile Synthesis of sub-nanometric copper clusters by double confinement enables selective reduction of carbon dioxide to methane, Angew. Chem. Int. Ed. 59 (2020) 19054–19059.

[42] R. Wang, Z. Li, H. Zheng, K. Xie. Kechang, Preparation of chlorine-free Cu/AC catalyst and its catalytic properties for vapor phase oxidative carbonylation of methanol, Chin. J. Catal. 31 (2010) 851–856.

[43] M. Ren, J. Ren, P. Hao, J. Yang, D. Wang, Y. Pei, J.Y. Lin, Z. Li, Influence of microwave irradiation on the structural properties of carbon-supported hollow copper nanoparticles and their effect on the synthesis of dimethyl carbonate, ChemCatChem 8 (2016) 861–871.

[44] J. Ren, W. Wang, D. Wang, Z. Zuo, J. Lin, Z. Li, A theoretical investigation on the mechanism of dimethyl carbonate formation on Cu/AC catalyst, Appl. Catal. A Gen. 472 (2014) 47–52.

[45] W. Sun, R. Shi, X. Wang, S. Liu, X. Han, C. Zhao, Z. Li, J. Ren, Density-functional theory study of dimethyl carbonate synthesis by methanol oxidative carbonylation on single-atom Cu_1/graphene catalyst, Appl. Surf. Sci. 425 (2017) 291–300.

[46] M. Peng, C. Dong, R. Gao, D. Xiao, H. Liu, Fully exposed cluster catalyst (FECC): toward rich surface sites and full atom utilization efficiency, ACS Cent. Sci. (2020).

[47] C. Jiang, J. Yang, T. Zhao, L. Xiong, Z.X. Guo, Y. Ren, H. Qi, A. Wang, J. Tang, Co^{3+}-O-V^{4+} cluster in CoVOx nanorods for efficient and stable electrochemical oxygen evolution, Appl. Catal. B Environ. 282 (2021), 119571.

[48] X. Hu, X. Fu, W. Wang, X. Wang, K. Wu, R. Si, C. Ma, C. Jia, C. Yan, Ceria-supported ruthenium clusters transforming from isolated single atoms for hydrogen production via decomposition of ammonia, Appl. Catal. B Environ. 268 (2020), 118424.

[49] L. Zhang, X. Cheng, G. Zhang, W. Qiu, H. He, G. Chen, High active platinum clusters on titanium dioxide supports toward carbon monoxide oxidation, Appl. Catal. B Environ. 266 (2020), 118629.

[50] M. Fan, W.D. Wang, Y. Zhu, X. Sun, F. Zhang, Z. Dong, Palladium clusters confined in triazinyl-functionalized COFs with enhanced catalytic activity, Appl. Catal. B Environ. 257 (2019), 117942.

[51] S.K. Cheah, L. Massin, M. Aouine, M.C. Steil, J. Fouletier, P. Gélin, Methane steam reforming in water deficient conditions on $Ir/Ce_{0.9}Gd_{0.1}O_{2-x}$ catalyst: Metal-support interactions and catalytic activity enhancement, Appl. Catal. B Environ. 234 (2018) 279–289.

[52] S.H. Lee, J.C. Lin, M. Farmand, A.T. Landers, J.T. Feaster, J.E. Avilés Acosta, J. W. Beeman, Y. Ye, J. Yano, A. Mehta, R.C. Davis, T.F. Jaramillo, C. Hahn, W. S. Drisdell, Oxidation state and surface reconstruction of Cu under CO_2 reduction conditions from in situ x-ray characterization, J. Am. Chem. Soc. (2020).

[53] J.A. Lupescu, J.W. Schwank, K.A. Dahlberg, C.Y. Seo, G.B. Fisher, S.L. Peczonczyk, K. Rhodes, M.J. Jagner, L.P. Haack, Pd model catalysts: effect of aging environment and lean redispersion, Appl. Catal. B Environ. 183 (2016) 343–360.

[54] M. Tang, W. Yuan, Y. Ou, G. Li, R. You, S. Li, H. Yang, Z. Zhang, Y. Wang, Recent progresses on structural reconstruction of nanosized metal catalysts via controlled-atmosphere transmission electron microscopy: a review, ACS Catal. 10 (2020) 14419–14450.

[55] J.A. Lupescu, J.W. Schwank, G.B. Fisher, J. Hangas, S.L. Peczonczyk, W.A. Paxton, Pd model catalysts: effect of air pulse length during redox aging on Pd redispersion, Appl. Catal. B Environ. 223 (2018) 76–90.

[56] K. Morgan, A. Goguet, C. Hardacre, Metal redispersion strategies for recycling of supported metal catalysts: a perspective, ACS Catal. 5 (2015) 3430–3445.

[57] P. Prslja, N. López, Stability and redispersion of ni nanoparticles supported on N-doped carbons for the CO_2 electrochemical reduction, ACS Catal. 11 (2021) 88–94.

[58] J. Chen, H. Wang, Z. Wang, S. Mao, J. Yu, Y. Wang, Redispersion of Mo-based catalysts and the rational design of super small-sized metallic Mo species, ACS Catal. 9 (2019) 5302–5307.

[59] J. Vavra, T. Shen, D. Stoian, V. Tileli, R. Buonsanti, Real-time monitoring reveals dissolution/redeposition mechanism in copper nanocatalysts during the initial stages of the CO_2 reduction reaction, Angew. Chem. 133 (2021) 1367–1374.

[60] H. Xu, D. Rebollar, H. He, L. Chong, Y. Liu, C. Liu, C. Sun, T. Li, J.V. Muntean, R. E. Winans, D. Liu, T. Xu, Highly selective electrocatalytic CO_2 reduction to ethanol by metallic clusters dynamically formed from atomically dispersed copper, Nat. Energy 5 (2020) 623–632.

[61] Y. Gao, X. Wu, S. Liu, M. Ogura, M. Liu, D. Weng, Aggregation and redispersion of silver species on alumina and sulphated alumina supports for soot oxidation, Catal. Sci. Technol. 7 (2017) 3524–3530.

[62] C.Y. Seo, X. Chen, K. Sun, L.F. Allard, G.B. Fisher, J.W. Schwank, Palladium redispersion at high temperature within the $Pd@SiO_2$ core@shell structure, Catal. Commun. 108 (2018) 73–76.

[63] Y. Jia, L. Zhang, A. Du, G. Gao, J. Chen, X. Yan, C.L. Brown, X. Yao, Defect graphene as a trifunctional catalyst for electrochemical reactions, Adv. Mater. 28 (2016) 9532–9538.

[64] Q. Lai, Q. Zheng, Z. Tang, D. Bi, J. Zhao, Y. Liang, Optimal configuration of N-doped carbon defects in 2D turbostratic carbon nanomesh for advanced oxygen reduction electrocatalysis research articles, Angew. Chem. 59 (2020) 11999–12006.

[65] Q. Cheng, C. Hu, G. Wang, Z. Zou, H. Yang, L. Dai, Carbon-defect-driven electroless deposition of Pt atomic clusters for highly efficient hydrogen evolution, J. Am. Chem. Soc. 142 (2020) 5594–5601.

[66] S. Sun, G. Zhang, N. Gauquelin, N. Chen, J. Zhou, S. Yang, W. Chen, X. Meng, D. Geng, M.N. Banis, R. Li, S. Ye, S. Knights, G.A. Botton, T.K. Sham, X. Sun, Single-atom catalysis using Pt/graphene achieved through atomic layer deposition, Sci. Rep. 3 (2013) 1–9.

[67] P. Tabib Zadeh Adibi, T. Pingel, E. Olsson, H. Grönbeck, C. Langhammer, Pt nanoparticle sintering and redispersion on a heterogeneous nanostructured support, J. Phys. Chem. C 120 (2016) 14918–14925.

[68] C. Kartusch, F. Krumeich, O. Safonova, U. Hartfelder, M. Makosch, J. Sá, J.A. Van Bokhoven, Redispersion of gold multiple-twinned particles during liquid-phase hydrogenation, ACS Catal. 2 (2012) 1394–1403.

[69] Q. Hu, Z. Han, X. Wang, G. Li, Z. Wang, X. Huang, H. Yang, X. Ren, Q. Zhang, J. Liu, C. He, Facile synthesis of sub-nanometric copper clusters by double confinement enables selective reduction of carbon dioxide to methane, Angew. Chem. Int. Ed. 59 (2020) 19054–19059.